ELSEVIER

A windowed Fourier pseudospectral method for hyperbolic conservation laws

Yuhui Sun [a], Y.C. Zhou [a], Shu-Guang Li [b], G.W. Wei [a,c,*]

[a] *Department of Mathematics, Michigan State University, East Lansing, MI 48824-1027, USA*
[b] *Department of Civil and Environmental Engineering, Michigan State University, MI 48824, USA*
[c] *Department of Electrical and Computer Engineering, Michigan State University, MI 48824, USA*

Abstract

A class of local spectral wavelet filters, discrete singular convolution (DSC) filters, is utilized to facilitate the Fourier pseudospectral method for the solution of hyperbolic conservation law systems. The DSC lowpass filters are adaptively implemented directly in the Fourier domain (i.e., windowed Fourier pseudospectral method), while a physical domain algorithm is also given to enable the treatment of some special boundary conditions. By adjusting the effective wavenumber region of the DSC filter, Gibbs oscillations can be removed effectively while the high resolution feature of the spectral method can be retained for a wide class of problems with various boundary conditions. The utility and effectiveness of the present approach are validated by extensive numerical experiments. The proposed method could operate at a resolution as high as only five points per wavelength (PPW) for the interaction of shocks and physical high frequency waves, which is some of the best for this class of problems. This high resolution, together with the low complexity of the fast Fourier transform (FFT), endows the proposed method considerable potential for solving large scale problems in hyperbolic conservation laws.
© 2005 Elsevier Inc. All rights reserved.

Keywords: Hyperbolic conservation laws; Fourier pseudospectral method; Discrete singular convolution; Local spectral wavelets; Adaptive lowpass filters; Gibbs oscillations

1. Introduction

It is well known that due to their accuracy and efficiency, spectral methods have great advantages over local methods in solving applicable scientific and engineering problems [4,7,10,33,43]. Given a hyperbolic system of nonlinear conservation laws

$$\mathbf{u}_t + \mathbf{f}(\mathbf{u})_x = 0 \tag{1}$$

with an initial condition

$$\mathbf{u}(x,0) = \mathbf{u}_0(x), \tag{2}$$

its solution may not exist in the classical sense because of possible discontinuities. The direct use of spectral methods to this problem will encounter Gibbs oscillations [15], which lead to blow-up in the time integration. Therefore, it has been of great interest in making spectral methods applicable to hyperbolic conservation law systems in the past two decades. The expectation is that the use of spectral methods will enable us not merely to capture the shock, but also to capture the delicate features and structures of the flow. Obviously, spectral approaches will be extremely valuable to a class of aerodynamic problems that involve the interaction of both turbulence and shock [28]. Such an interaction is some of the most challenging problems in computational fluid dynamics (CFD). Moreover, spectral approaches are some of the most efficient methods for challenging problems in heterogeneous groundwater modeling and simulation [31,32].

The main objective of many previous studies is to recover smooth solutions from those that are contaminated by the Gibbs oscillations and, meanwhile, to improve the rate of convergence. For shock-capturing, many up-to-date local methods, such as weighted essentially non-oscillatory (WENO) scheme [22,38], central schemes [3,26,30,35], arbitrary-order non-oscillatory advection scheme [42], gas kinetic [50], anisotropic diffusion [36] and image processing based schemes [17,48], perform well. The success of these local shock-capturing schemes lies in their appropriate amount of intrinsic numerical dissipation, which is introduced either by explicit artificial viscosity, upwinding, appropriate local average (non-oscillatory central schemes), or by relaxation [23]. The characteristic decomposition based on Roe's mean matrix can also be considered as a local average of the Jacobian matrix $A(u) = \partial f(u)/\partial u$. In their recent work, LeVeque and Pelanti [29] outlined the relation between some approximate Riemann solvers and relaxation schemes. The relative amount of numerical dissipation may explain why the local characteristic decomposition is not necessary in low-order methods while it seems to be indispensable in high-order methods [38]. However, when these local methods are used in cases where flow structures with fine details are needed to be resolved together with shocks, numerical dissipation is usually found to be so large that the fine detail might be smeared. Spectral methods, on the contrary, contribute very little numerical dissipation and dispersion in principle when used to approximate spatial derivatives of a smooth function. Nevertheless, when they are applied to the approximation of spatial derivatives of a discontinuous function, Gibbs oscillations again have to be suppressed by appropriate means, for which there are two general approaches: (1) explicit artificial viscosity, e.g. spectral viscosity (SV) method proposed by Tadmor [40], and (2) filtering [1,34]. The latter is the central issue of the present study.

At present, most filters are constructed in the spectral domain and they can be called spectral filters. Typical spectral filters are Lanzos filter, raised cosine filter, sharpened raised cosine filter and exponential cutoff filter, as listed by Hussaini et al. [21]. More sophisticate and effective filters in spectral domain are Vandeven's pth order filter [44], Cai et al.'s sawtooth function [5], and Gottlieb and Tadmor's regularized Dirichlet function [14]. A successful nonlinear filter was introduced by Krasny to suppress the spurious growth of roundoff errors in the numerical evolution of vortex sheets [25]. The Krasny filter removes all Fourier modes lying below certain tolerance and leaves those lying above the tolerance unchanged. Krasny was able to accurately integrate numerical solutions essentially up the time they become singular. Shyy and his coworkers [24] have shown that a filter-based Reynolds-averaged Navier–Stokes (RANS) approach improves the predictive capability considerably in comparison to the standard k–ϵ model.

Apart from methods that are implemented in the spectral domain, filters in the physical domain are also developed. It is generally more difficult to design appropriate filters in the physical domain than in the Fourier domain. A straightforward procedure is to make use of numerical dissipation partially contained in some *high-order* shock-capturing schemes [6], such as the ENO scheme, where, actually, numerical dissipation was introduced both in the Fourier domain (via an exponential filter) and in the physical domain (via ENO polynomial interpolation). Such a strategy was generalized by Yee et al. [52] for constructing characteristic filters in the framework of finite difference or finite volume methods. Their method has been successfully applied to shock-capturing and turbulence simulations. Another procedure was initiated by Gottlieb and Shu [15] by using the Gegenbauer polynomial to resolve the oscillatory partial Fourier summation. Some promising numerical results from filter approaches can be found in [8,9,16].

Nevertheless, some prominent issues may hinder the success of filtered spectral methods for practical numerical computations involving shocks. In our view, there are two very important issues that are vital to the success of filtered spectral schemes. The first issue is how to select optimal filters for shock-capturing. The issue is very intricate and cannot have a unique solution at this point because there are so many properties to mind, such as flatness, ripple, filter length, effective frequency range and length of transition band, to name only a few. In general, it is desirable to have filters that are free of dispersion errors, flat while having very small transition band, short in length while having high resolution. Moreover, what adds to the complexity is that solutions to different hyperbolic conservation law systems may have different Fourier spectral distributions. Consequently, one faces the difficulty that an optimal filter for one problem may not even work for another one. Therefore, it is desirable to have a filter which accounts for this change by very few adjustable parameters.

The second issue concerns the change of solution with respect to the time evolution for a given hyperbolic conservation law system. As the Fourier spectral distribution of a given problem changes with time, the question is how to implement the filter to reflect the change. It will be too dissipative for many systems if a filter is applied at each time step of the integration. Therefore, an adaptive implementation, which is controlled by a sensor during the time integration, is appropriate. Given the complexity, it is unlikely that there will be an ideal solution to these issues in the immediate future. Obviously, these challenging and interesting problems call for the further study of spectral filter approaches.

To put the matter in perspective, there is no such a method that is perfect for all tasks in hyperbolic conservation laws. In general, high order methods, including spectral methods, are desirable for problems with natural high frequency oscillations. However, they can be out performed by low order schemes for problems whose Fourier responses of the solution focus predominantly on the low frequency range. For this class of problems, first order or second order Godunov type of schemes can be more efficient in balancing accuracy and CPU time. Moreover, many high order shock-capturing methods were found to be too dissipative to be applicable for the long-time integration of the interaction of shock waves and turbulence [12]. In the framework of free decaying turbulence, the excessive dissipation degrades the numerical resolution, smears small-scale structures and masks the effect of a subgrid-scale model [12]. To reduce the excessive numerical dissipation, a local shock sensor can be employed [48]. Another approach is to design adaptive filters [18,27,49,54,55]. Hill and Pullin [20] constructed a hybrid method combining a tuned central difference with the WENO for use in the LES of strongly compressible, shock-driven flows. They found that practically a switch is necessary to maintain good performance [20]. Therefore, giving the fact that there are so many different problems arisen from a vast variety of physical origins, it is often more advantageous to have one or two tunable parameters so that a general shock-capturing scheme can adapt to various problems.

Recently, an adaptive conjugate filter oscillation reduction (CFOR) scheme [18,49,54,55] was proposed for hyperbolic conservation laws. The CFOR scheme was constructed within the framework of the discrete singular convolution (DSC) algorithm [45–47], which is a local spectral wavelet method for solving partial differential equations. By 'conjugate filters' it means that the effective wavenumber range of the lowpass filter is largely overlapped with that of the highpass filter used for the approximation of spatial derivatives. The CFOR scheme has been extensively validated over a wide range of shock-capturing problems [18,49,54,55]. It provides some of the highest grid resolution, i.e., 5 points per wavelength (PPW), for the interaction of shock and entropy waves, and for many other challenging problems involving natural high frequency oscillations [54,55]. The success of the CFOR lies in the adaptive implementation of the conjugate lowpass filter to control unphysical oscillations.

The objective of this work is to construct, analyze and implement a class of adaptive DSC lowpass filters in the framework of the Fourier pseudospectral method (FPM) for suppressing Gibbs oscillations. Since the DSC lowpass filters are constructed by regularizing Dirichlet type of kernels, it is expected that they match very well with the frequency range of the FPM. In fact, the DSC lowpass filters have a sufficiently wide effective wavenumber range that makes it viable to capture fine flow structures, which is a desirable objective of spectral methods for hyperbolic conservation law systems. It is this effective wavenumber range that controls the resolution of the overall scheme. In our design, this effective range can be varied by a parameter according to the resolution requirement of a problem under study. Different DSC kernels have different magnitude responses and adjustability in the Fourier domain, which in turn influence the accuracy and resolution. It is this flexibility that makes the proposed method applicable to a wide variety of shock capturing problems.

These filters can be implemented in either the physical domain or the Fourier domain. The resulting Fourier domain algorithm is essentially a *windowed Fourier pseudospectral method* (WFPM) that is capable of shock-capturing.

The rest of this paper is organized as follows. In Section 2, a brief introduction will be devoted to the construction of the DSC lowpass filters followed by a discussion of two types of implementations of these filters with spectral methods. Extensive numerical experiments are carried out in Section 3, including Burgers' equation, shock-tube problems, shock–entropy wave interaction, shock–vortex interaction and flow past a cylinder. The shock-capturing ability and the high resolution feature of the present method are addressed. Section 4 is devoted to a discussion of experimental results. Advantages and disadvantages of different methods are analyzed. A concluding remark ends this paper.

2. Theory and algorithm

We first discuss the construction of DSC lowpass filters. Then the implementation of these filters in both the Fourier domain and the physical domain is described.

2.1. DSC lowpass filter

In the context of distribution theory, a singular convolution is defined by

$$f(x) = (T * \eta)(x) = \int_{-\infty}^{\infty} T(x - t)\eta(t)\, \mathrm{d}t, \tag{3}$$

where $T(x)$ is a singular kernel and $\eta(x)$ is an element of the space of test functions. Interesting singular kernels include that of the Hilbert type, Abel type and delta type. The former two play important roles in the theory of analytical functions, processing of analytical signals, theory of linear responses and Radon transform. Since delta type kernels are the key element in the theory of approximation and the numerical solution of differential equations, we focus on singular kernels of the delta type

$$T(x) = \delta^{(q)}(x), \quad q = 0, 1, 2, \ldots, \tag{4}$$

where superscript (q) denotes the qth-order 'derivative' of the delta distribution $\delta(x)$, with respect to x, which should be understood as generalized derivatives of distributions. When $q = 0$, kernel $T(x) = \delta(x)$ is important for the interpolation of functions. In this work, only the case of $q = 0$ will be involved. However, one has to find appropriate approximations to the above singular kernel, which cannot be directly realized in computers. To this end, we consider a sequence of approximations

$$\lim_{\alpha \to \alpha_0} \delta_\alpha^{(q)}(x) = \delta^{(q)}(x), \quad q = 0, 1, 2, \ldots, \tag{5}$$

where α is a parameter which characterizes the approximation with the α_0 being a generalized limit. Among various candidates of approximation kernels [46], regularized Shannon kernel (RSK)

$$\delta_{\sigma,\Delta}(x) = \frac{\sin \frac{\pi}{\Delta} x}{\frac{\pi}{\Delta} x} \exp\left(-\frac{x^2}{2\sigma^2}\right) \tag{6}$$

is frequently used due to its close link to the Shannon wavelet scaling function. In this formula, Δ is the grid spacing and σ determines the width of the Gaussian envelop. For a given $\sigma \neq 0$, the limit of $\Delta \to 0$ reproduces the delta kernel (distribution). With the RSK, a function u can be approximated by a discrete convolution

$$u(x) \approx \sum_{k=\lceil x \rceil - W}^{\lceil x \rceil + W} \delta_{\sigma,\Delta}(x - x_k)u(x_k), \quad q = 0, 1, 2, \ldots, \tag{7}$$

where $\lceil x \rceil$ denotes the grid point that is closest to x, and $2W + 1$ is the computational bandwidth, or effective kernel support, which is usually smaller than the computational bandwidth of the spectral method, i.e., the entire domain span. Normally, a larger W will lead to a higher resolution. We set $W = 32$ in this work. Eq. (7) is often referred as a DSC. The RSK is employed as a prototype of a DSC lowpass filter. Certainly,
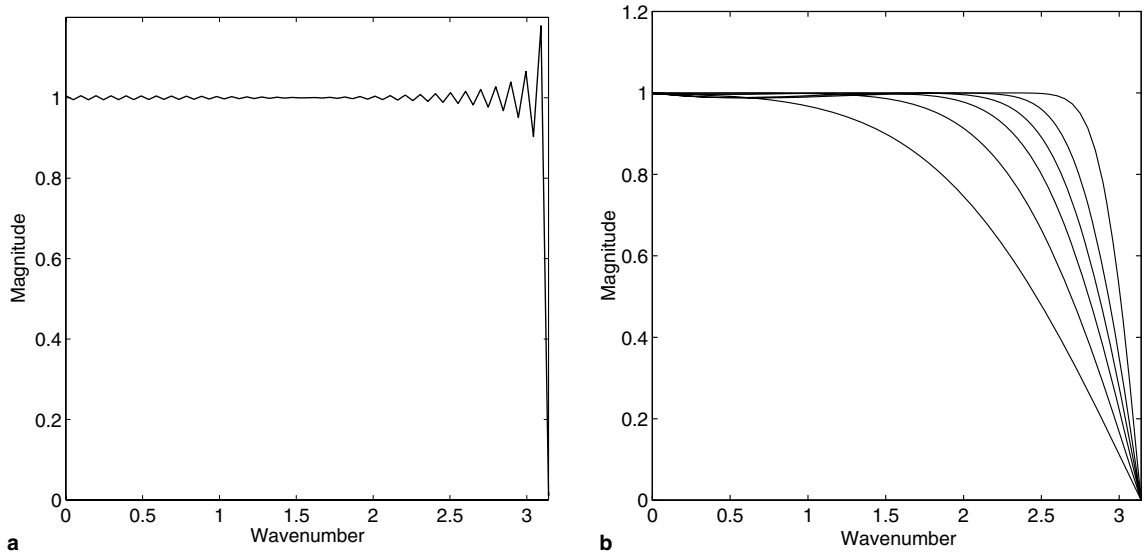
Fig. 1. The Fourier magnitude response of lowpass filters. (a) The Shannon filter. (b) The DSC-RSK filter. $r = 1.0, 1.5, 2.0, 2.5, 3.2, 5.0$ from the left to right.

many other DSC kernels, such as the Hermite polynomial based DSC kernel [53], can be similarly employed [55]. Mathematical analysis [37] indicates that the RSK is a local spectral kernel.

Fig. 1(a) shows the Fourier magnitude response of the truncated Shannon (i.e., sinc) kernel. As the Shannon kernel is interpolative, i.e., it is zero on grid points except for $x = 0$, we compute its Fourier transform by using its values on $\{x_{j+\frac{1}{2}}\}_{j=0}^{31}$. Obviously, dramatic oscillations in the passband disqualify the truncated Shannon kernel as useful lowpass filter for high precision computations. Small oscillations in the filter frequency response could induce large error in the long time integration of conservation law systems. In Fig. 1(b), we plot the Fourier frequency response of the DSC-RSK lowpass filters, $\delta_{\sigma,\Delta}(x_{j+\frac{1}{2}})$, $j = 0, 1, \ldots, 31$, at a number of different r values. These profiles are obtained in the same manner as that for the Shannon kernel. The feasibility of the DSC-RSK as lowpass filters in numerical computations is based on an important observation: by adjusting the ratio $r(r = \frac{\sigma}{\Delta})$ of the regularizer, one can suppress the oscillation and control the effective wavenumber region, i.e., the range of wavenumbers that the filter value is unit. The size of effective wavenumber region determines the resolution of the lowpass filter.

The selection of the filter parameter r is quite complicated. On the one hand, to avoid oscillations in filter frequency response, r value should not be too large. On the other hand, if r value is too small, then the filter will be too dissipative and its numerical resolution will be very low. In the between, there is a wide range of r values as shown in Fig. 1(b). However, there is no such r that is optimal for all the problems in hyperbolic conservation laws. The best selection of r for a given problem depends on the knowledge and understanding of the problem. In fact, if one can estimate the Fourier spectrum distribution of the solution of the problem under study, one can easily choose a suitable r value such that effective wavenumber region of the filter covers the nontrivial part of the Fourier spectrum distribution. If one knows little about the physics of the problem, one has to try a few different r values and compare their outcome.

2.2. Fourier domain algorithm

We denote $\zeta_r(x_{j+\frac{1}{2}}) = \delta_{\sigma,\Delta}(x_{j+\frac{1}{2}})$ the proposed DSC-RSK lowpass filter in the physical domain $[0, L]$ and $\hat{\zeta}_r(\omega_n)$ its image in the Fourier domain, where $\Delta = L/N$, $x_j = j\Delta$ and $\omega_n = \frac{2\pi n}{L}$. Here, we define only the middle-grid filter because the interpolative filter cannot be used directly on grid. The obvious relation between $\zeta_r(x_{j+\frac{1}{2}})$ and $\hat{\zeta}_r(\omega_n)$ is

$$\hat{\zeta}_r(\omega_n) = \Delta \sum_{j=0}^{N-1} \zeta_r(x_{j+\frac{1}{2}}) e^{-i\omega_n x_j}. \tag{8}$$

Filtering in the Fourier domain is usually accomplished by multiplying the given Fourier coefficients $\hat{u}(\omega_n) = \Delta \sum_{j=0}^{N-1} u(x_j) e^{-i\omega_n x_j}$ by $\hat{\zeta}_r(\omega_n)$ directly, i.e., a windowed Fourier transform,

$$u^{\zeta}(x_j) = \frac{1}{L} \sum_{n=-\frac{N}{2}}^{\frac{N}{2}-1} \hat{\zeta}_r(\omega_n) \hat{u}(\omega_n) e^{i\omega_n x_j}. \tag{9}$$

Therefore, the *modified* Fourier coefficients $\hat{\zeta}(\omega_n)\hat{u}(\omega_n)$ in Eq. (9) are the Fourier coefficients of a *localized* version of the original function $u(x_j)$: $u^{\zeta}(x_j)$. Hence, errors arising from the discontinuity are also localized and the accuracy away from the discontinuity can be ensured. In practical applications, one only needs to carry out the filtering and differentiation $D_x u = u_x$ in one step

$$u_x^{\zeta}(x_j) = \frac{1}{L} \sum_{n=-\frac{N}{2}}^{\frac{N}{2}-1} i\omega_n \hat{\zeta}_r(\omega_n) \hat{u}(\omega_n) e^{i\omega_n x_j}. \tag{10}$$

This is essentially a windowed Fourier transform (WFT) for calculating the derivatives of a function u. In the present work, the standard fourth-order Runge–Kutta (RK-4) scheme is employed for the time advancing. We use a TVD switch to adaptively activate the application of the DSC-RSK lowpass filter. Whenever the total variation of the approximate solution in the two consecutive time steps exceeds a prescribed criterion, the lowpass filter is activated. The DSC-RSK lowpass filter is only applied at the end of each full RK-4 cycle. The reader is referred to our earlier work [18,49,54,55] for the detail of this adaptive filtering.

2.3. Physical domain algorithm

It is more difficult to apply the filter in the physical domain than in the Fourier domain. On one hand, it is not easy to quantitatively analyze the influence of numerical dissipation in the physical domain. On the other hand, the convolution operation

$$u^{\zeta}(x) = \int u(x - \xi)\zeta_r(\xi) \, d\xi \tag{11}$$

complicates the physical domain application of the filter. However, in some practical applications, it turns out to be quite necessary to implement the filter in the physical domain, especially for problems whose boundaries require some special treatments. To implement two reflective boundaries in the frequency domain algorithm, one has to use a computational domain which is three time as large as the original one. Therefore, we also propose a method to employ our DSC-RSK lowpass filter in the physical domain. Due to the fact that the RSK lowpass filter is an interpolation kernel, we consider a two-step procedure. The first step is the prediction of middle-grid values from the nodal values

$$u^{\zeta}(x_{i+\frac{1}{2}}) = \sum_{j=i-W}^{i+W-1} \zeta_r(x_{i+\frac{1}{2}} - x_j) u(x_j). \tag{12}$$

The second step is the reconstruction of the nodal values from the middle-grid values

$$u^{\zeta\zeta}(x_i) = \sum_{j=i-W}^{i+W-1} \zeta_{r'}(x_i - x_{j+\frac{1}{2}}) u^{\zeta}(x_{j+\frac{1}{2}}), \tag{13}$$

where r' normally differs from r. It turns out that we need to use a small r value in only one of these two steps. A relatively large value, say $r = 3.5$ is used in the other step. The activation of the RSK lowpass filter is controlled in the same manner as that of the frequency domain algorithm [18,49,54,55].

As described, the DSC-RSK lowpass filter can be applied either in the physical domain or in the Fourier domain. In general, filtering in the Fourier domain is much easier and more convenient than that in the

physical domain because no additional computation is required to implement the filter in the Fourier spectral method. In contrast, the physical domain implementation requires two additional summations. Therefore, we have used the filter in the Fourier domain in most of our numerical experiments except for the cases in which reflective and out-flow boundary conditions are involved. We have checked that whenever applicable, results obtained from the Fourier domain approach are identical to those from the physical domain approach.

2.4. Post-processing filter

Cosmetic post-processing was introduced by Gottlieb et al. [13] to make the solution more presentable once the entire time integration has completed. In particular, for problems where only weak smoothing is needed for stabilizing, a strong post-processing filter is routinely used in the literature. We have adopted this procedure in our numerical experiments. In principle, we can achieve the post-processing by reducing the *r* value of the DSC-RSK lowpass filter at the last time step of the computation. As an alternative, we provide a series of lowpass filters based on the Lagrange delta kernel which is given by

$$L_W(x, x_j) = \prod_{k=-W, k \neq j}^{W} \frac{x - x_k}{x_j - x_k}, \quad j = -W, \dots, W. \tag{14}$$

Fig. 2 shows the Fourier magnitude response of the Lagrange delta kernel. In fact, the highpass versions of these filters are graphically identical to centered finite difference (FD) schemes. In our numerical experiments, we adopt Lagrange-2 or Lagrange-4 as post-processing filters.

3. Numerical experiments

In this section, we examine the validity and demonstrate the performance of the proposed windowed (filtered) Fourier pseudospectral scheme for conservation law systems. In the present study, a large collection of standard linear and nonlinear benchmark problems is considered, including the linear advection equation, 1D inviscid Burgers' equation, shock tube (Sod and Lax) problems, 1D shock–entropy interaction, 2D shock–entropy
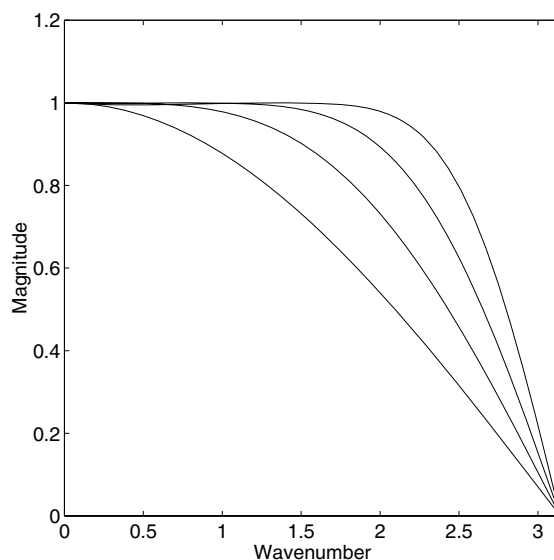

Fig. 2. The Fourier magnitude response of the Lagrange filter. Lagrange-2, Lagrange-4, Lagrange-8 and Lagrange-16 from the left to right.

interaction, 2D shock–vortex interaction, 2D advection of an isentropic vortex, and flow past a cylinder. Some of these problems have periodic boundary conditions therefore the windowed Fourier pseudospectral method can be applied directly. For problems whose boundary conditions are not periodic, we symmetrically double the computational domain to compute the flux derivative. It is noted that the domain extension is necessary for converting a non-periodic problem into a periodic one suitable for the Fourier pseudospectral method. Our filtering procedures, as described earlier, can be applied with general boundary conditions, such as Dirichlet or Neumann. In this work, we have adopted the conservative variable formulation. Therefore, for convenience, filters are applied to the conservative variables, instead of primitive ones. In Appendix I, we list the filter parameter r used for each numerical example.

3.1. Scalar conservation law systems

We begin our numerical experiments with the scalar conservation law system, which is given by

$$u_t + f(u)_x = 0, \tag{15}$$

where $f(u)$ is a function of u. It is generally believed that spectral methods are not very suitable for scalar conservation law systems with simple shock profiles, and should not be used if one is interested primarily in the shock profiles rather than other the detailed structure of the flow. Contrary to the general belief, we demonstrate that the proposed global spectral scheme in fact performs well for this class of localized shock problems.

Example 1. We first solve a linear advection equation, which is of the form

$$\begin{aligned} u_t + u_x &= 0, \quad -1 < x < 1, \\ u(x,0) &= u_0(x), \quad \text{periodic}, \end{aligned} \tag{16}$$

where u_0 is an initial value

$$u_0(x) = \begin{cases} \frac{1}{6}\left(G(x,\beta,z-\delta) + G(x,\beta,z+\delta) + 4G(x,\beta,z)\right), & -0.8 \leqslant x \leqslant -0.6, \\ 1, & -0.4 \leqslant x \leqslant -0.2, \\ 1 - |10(x - 0.1)|, & 0 \leqslant x \leqslant 0.2, \\ \frac{1}{6}\left(F(x,\alpha,a-\delta) + F(x,\alpha,a+\delta) + 4F(x,\alpha,a)\right), & 0.4 \leqslant x \leqslant 0.6, \\ 0, & \text{otherwise}. \end{cases} \tag{17}$$

Functions G and F are defined as

$$\begin{aligned} G(x,\beta,z) &= e^{-\beta(x-z)^2}, \\ F(x,\alpha,a) &= \sqrt{\max(1 - \alpha^2(x-a)^2, 0)}, \end{aligned} \tag{18}$$

where $a = 0.5$, $z = -0.7$, $\delta = 0.005$, $\alpha = 10$ and $\beta = \frac{\log 2}{36\delta^2}$.

The solution of this problem contains a combination of a Gaussian, a square wave, a sharp triangle wave and a half ellipse. The exact solution at any time can be easily obtained by a translation of the initial solution at the unit speed. In Figs. 3 and 4, we display the numerical results for this problem at $t = 8$ with 128 and 256 grid points, respectively. We observe that our method works well in both cases.

Example 2. Secondly, we test the proposed method by considering a moving W-shape wave, i.e., a piecewise continuous initial value, for the linear advection equation [49]

$$u_0(x) = \begin{cases} 1, & 0 \leqslant x \leqslant 0.2, \\ 4x - \frac{3}{5}, & 0.2 \leqslant x \leqslant 0.4, \\ -4x + \frac{13}{5}, & 0.4 \leqslant x \leqslant 0.6, \\ 1, & 0.6 \leqslant x \leqslant 0.8. \\ 0, & \text{otherwise}. \end{cases} \tag{19}$$
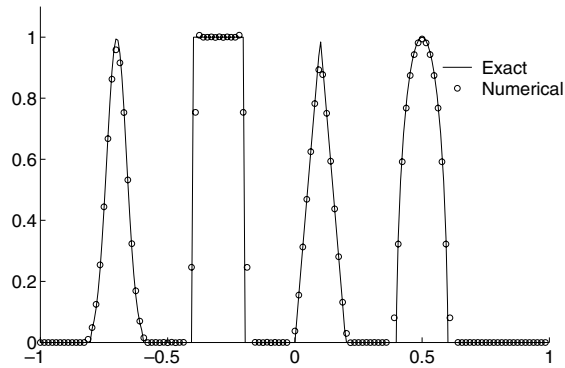
Fig. 3. Solution of the linear advection equation. $t = 8$, $\Delta t = 0.001$, 128 grid points.
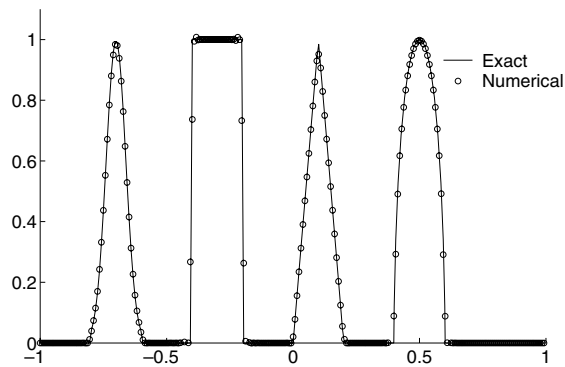

Fig. 4. Solution of the linear advection equation. $t = 8$, $\Delta t = 0.001$, 256 grid points.

This case is very similar to Example 1 but contains so-called contact discontinuity and is quite difficult to resolve in hyperbolic conservation laws. In particular, the interaction of two lines at $x = 0.2$ and $x = 0.6$ is difficult to resolve. Hence, it is a good test for the shock-capturing ability of the present method. We compute the solution up to $t = 8$. Our results are shown in Figs. 5 and 6.

Example 3. Having solved the linear equation with different initial values, we consider the solution of the most popular model, inviscid Burgers' equation, in which $f(u) = u^2/2$ and the Riemann type initial value is given by

$$u(x,0) = \begin{cases} 1, & x \leqslant 0, \\ 0, & x > 0. \end{cases} \tag{20}$$

This is a standard benchmark problem in hyperbolic conservation laws and has been considered by numerous researchers. The exact solution is a shock wave with a constant velocity

$$u(x,t) = \begin{cases} 1, & x - St < 0, \\ 0, & x - St > 0, \end{cases} \tag{21}$$

where the speed of the shock front is

$$S = \frac{1}{2}. \tag{22}$$

It is noted that this is a problem with non-periodic boundary condition. We must symmetrically double the computational domain in the x-direction when we calculate the derivative of the flux. This operation is
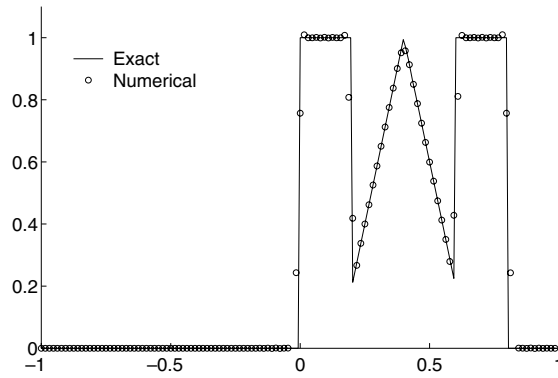
Fig. 5. Solution of the linear advection equation. $t = 8$, $\Delta t = 0.001$, 128 grid points.
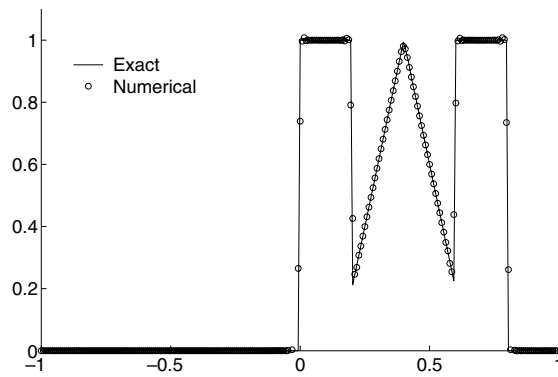

Fig. 6. Solution of the linear advection equation. $t = 8$, $\Delta t = 0.001$, 256 grid points.

necessary because it generates the periodic boundary condition so that the Fourier pseudospectral method can be used. The numerical results are plotted in Fig. 7 at time $t = 2$.

Example 4. Another Riemann type initial value for inviscid Burgers' equation with the flux of $u^2/2$ is given by

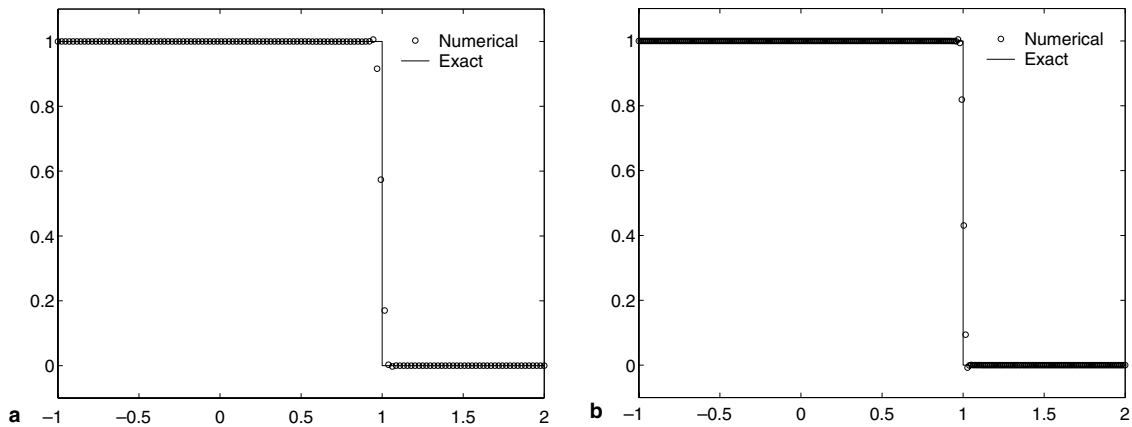$$u(x,0) = \begin{cases} 0, & x < 0, \\ 1, & x \geqslant 0. \end{cases} \tag{23}$$

Fig. 7. Solution of inviscid Burgers' equation ($t = 2$, $\Delta t = 0.005$): (a) 129 grid points; (b) 257 grid points.

The exact solution of this problem is a rarefaction wave

$$u(x,t) = \begin{cases} 0, & \frac{x}{t} < 0, \\ \frac{x}{t}, & 0 < \frac{x}{t} < 1, \\ 1, & \frac{x}{t} > 1. \end{cases} \tag{24}$$

Fig. 8 shows the numerical result of this problem at $t = 2$ with different mesh grids. It can be observed that the end of the rarefaction fan has been well resolved.

Example 5. Finally, we choose the problem with a non-convex flux to test the convergence to the physically correct solution. The flux is a non-convex function

$$f(u) = \frac{1}{4}(u^2 - 1)(u^2 - 4) \tag{25}$$

with a Riemann initial condition

$$u(x,0) = \begin{cases} -3, & x < 0, \\ 3, & x \geqslant 0. \end{cases} \tag{26}$$

We refer the reader to the work of [19] for the exact solution and more detailed information about this problem. This problem is relatively difficult. In the literature, commonly reported numerical result is given at $t = 0.04$ [22]. Our result is displayed in Fig. 9. Again, the present Fourier pseudospectral solver yields a satisfactory resolution.

3.2. 1D Euler system

In this subsection, we perform numerical experiments by using the proposed scheme for the 1D Euler equation of gas dynamics. In one dimension, the Euler equation takes the form

$$U_t + F(U)_x = 0 \tag{27}$$

with

$$U = \begin{pmatrix} \rho \\ \rho u \\ E \end{pmatrix}, \quad F(U) = \begin{pmatrix} \rho u \\ \rho u^2 + p \\ u(E + p) \end{pmatrix}, \tag{28}$$
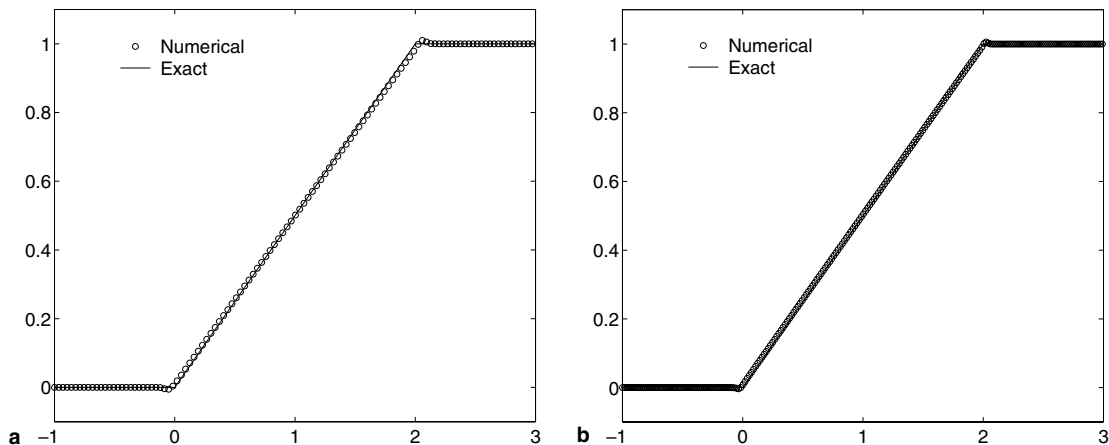

Fig. 8. Solution of inviscid Burgers' equation with rarefaction wave ($t = 2$, $\Delta t = 0.005$): (a) 129 grid points; (b) 257 grid points.
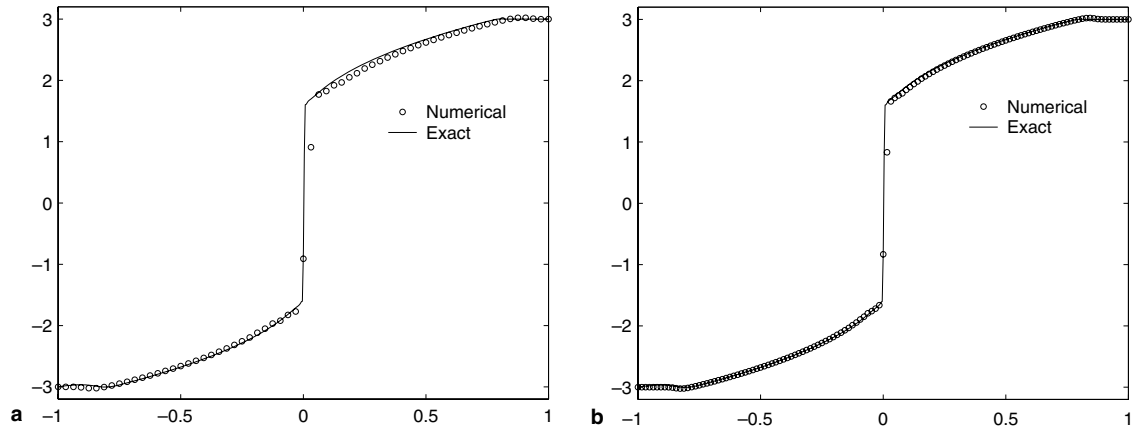
Fig. 9. Solution of inviscid Burgers' equation with non-convex flux ($t = 0.04$, $\Delta t = 0.0005$): (a) 65 grid points; (b) 129 grid points.

where, ρ, u, p and E denote the density, velocity, pressure and total energy per unit mass $E = \rho[e + (u^2)/2]$, respectively. Here, e is the specific internal energy. For an ideal gas with the constant specific heat ratio ($\gamma = 1.4$) considered here, one has $e = p/(\gamma - 1)\rho$. We consider the following two well-known Riemann problems.

Example 6. Two shock tube problems, i.e., Sod's problem and Lax's problem, are standard tests. Their initial conditions are given by

$$(\rho, u, p)_{t=0} = \begin{cases} (1, 0, 1), & x < 0, \\ (0.125, 0, 0.1), & \text{otherwise} \end{cases} \tag{29}$$

for Sod's problem and

$$(\rho, u, p)_{t=0} = \begin{cases} (0.445, 0.698, 3.528), & x < 0, \\ (0.5, 0, 0.571), & \text{otherwise} \end{cases} \tag{30}$$

for Lax's problem. In fact, these problems favor low-order shock capturing schemes. The numerical results for these two problems are shown in Figs. 10 and 11, respectively. We can see that the present method gives a good resolution in both cases. Similar to the performance of other methods depending on the numerical dissipation, the resolution of the present method for the linear degenerate contact discontinuity is slightly lower than that for the generic nonlinear shock wave.
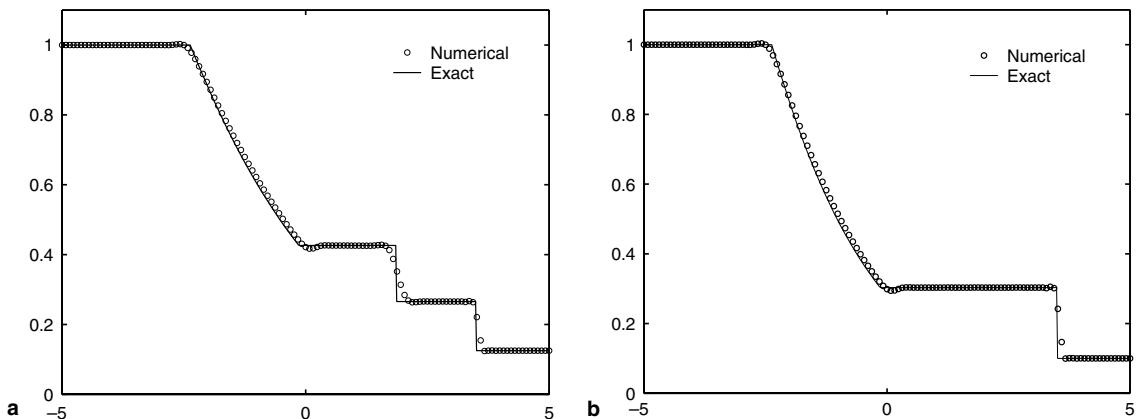

Fig. 10. Solution of Sod's problem ($t = 2$, $\Delta t = 0.02$, 129 grid points): (a) density; (b) pressure.
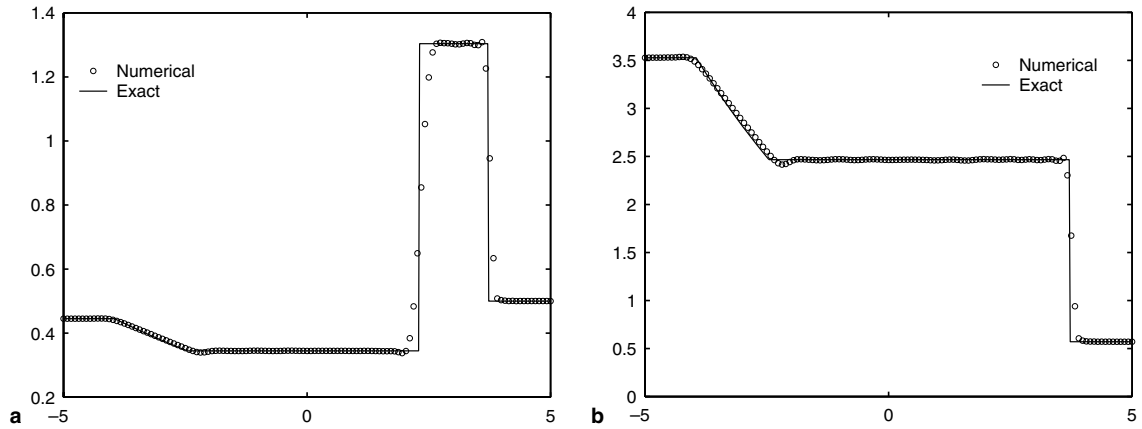
Fig. 11. Solution of Lax's problem ($t = 1.5$, $\Delta t = 0.02$, 129 grid points): (a) density; (b) pressure.

Example 7. We now consider the interaction of an entropy wave of small amplitude with a Mach 3 right-moving shock in a one-dimensional flow. The flow field is initialized with

$$(\rho, u, p)_{t=0} = \begin{cases} (3.85714, 2.629369, 10.33333), & x \leqslant 0.5, \\ (e^{-\epsilon \sin(\kappa x)}, 0, 1.0), & x > 0.5 \end{cases} \qquad (31)$$

on a domain $[0, 9]$. Here ϵ and κ are the amplitude and the wave number of the entropy wave before the shock. This problem is significant due to its relevance to the interaction of shock-turbulence. Spectral methods, by nature of their high accuracy and negligible errors of dispersive and dissipative, are ideally suited to the numerical study of turbulence. Here we would like to argue the feasibility of the present spectral method to the shock-turbulence interaction. In our test, we vary the wavenumber of the pre-shock wave while keeping its amplitude unchanged ($\epsilon = 0.01$). As the wavenumber increases, the problem becomes more and more challenging because the amplified high-frequency entropy waves after the shock are always mixed with spurious oscillations. As the wavenumber increases, it is very difficult to distinguish the high-frequency waves from spurious oscillations. A low-order scheme may dramatically damp the transmitted high frequency waves. Even some popular high-order schemes also encounter the difficulty in preserving the amplitude of the entropy wave due to their excessive dissipation with a given mesh size. Therefore, a successful shock-capturing method should be able to eliminate Gibbs' oscillations, capture the shock and preserve the high-frequency entropy wave [54].

In our test, we let the shock move from $x = 0.5$ to $x = 8.5$. For the purpose of a comparison with previous results, we only give the results at interval $[4.0, 9.0]$. Moreover, in order to discharge transient waves due to the non-numerical initial shock profile, we plot the length of the amplified entropy waves in the same manner as that in [22]. Furthermore, we must point out two non-trivial details for the following cases with different κ. One is that the plotted results are obtained by an interpolation of our final numerical results from a coarse grid to a denser grid. This is necessary because our computational grid is too coarse to show the peaks and valleys of our numerical results. The other is that we have used a local filter as described in Section 2.4 to eliminate the oscillations near the shock when we present the final result after the full computation.

First, we consider $\kappa = 18$. In this case, the computational domain is deployed with 513 grid points. Such a mesh is suitable for the Fourier pseudospectral method. The amplitudes of the entropy waves are shown in Fig. 12(a). It can be seen that the shock and the generated entropy waves are ideally captured. Two solid lines at ± 0.08690716 are predicted by the linear analysis, and confine the amplitude of the amplified entropy waves. Our entropy waves fully span the strip bounded by the solid lines. The transmitted waves suffer the similar smearing as the contact waves. The shock wave, on the contrary, is self-repairable due to its compression nature. This observation verified that the numerical dissipation needed for shock-capturing will degenerate the
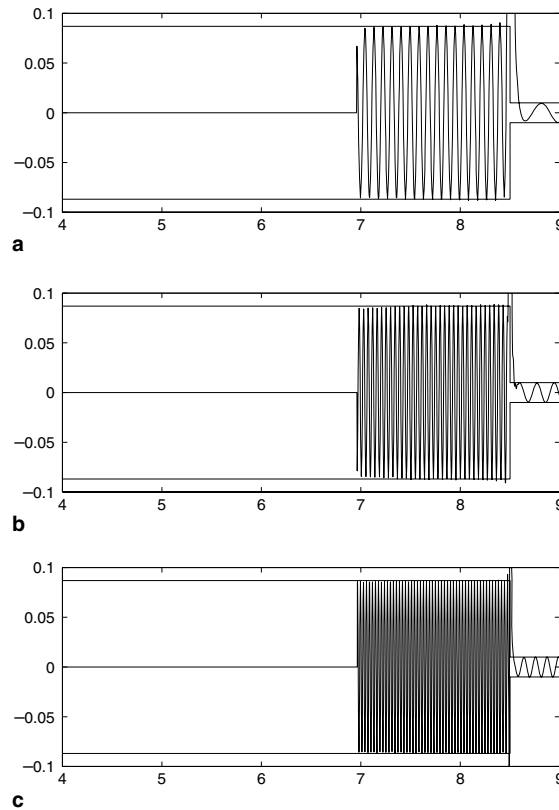
Fig. 12. The interaction of 1D shock and entropy waves. The amplitude of entropy waves: (a) $\kappa = 18$, $N = 513$; (b) $\kappa = 36$, $N = 1025$; (c) $\kappa = 54$, $N = 2049$.

resolution of the spectral method. It also verified that this degeneration can be isolated and alleviated by the DSC-RSK filter.

Since post-shock waves are monochromic, a simple calculation indicates that the resolution is about 5 points per wavelength (PPW), which is similar to that of our previous CFOR scheme [54,55]. Such a resolution is lower than the Nyquist limit, i.e., 2 PPW, but it is much higher than that could be obtained by most other existing shock-capturing schemes in the literature.

We next double the wave number κ up to 36. A mesh of 513 grid points is not enough for simultaneous shock capturing and high-frequency wave resolving. Therefore, we increase the mesh size to $N = 1025$ for this computation. The same resolution, i.e., 5 PPW, is maintained in this high-frequency wave case. The result is presented in Fig. 12(b). It is observed that no obvious deterioration occurs to the result and the resolution in the post-shock waves is still satisfactory. The amplitude of the waves fully spans the confining lines, as in the case of $\kappa = 18$. However, the first post-shock wave has been slightly polluted.

When the wave number κ is increased to 54, we use 2049 grid points to resolve such high-frequency waves. Fig. 12(c) shows the result of $\kappa = 54$. The resolution is about 7.5 PPW in this simulation, which is still much higher than that could be achieved by other existing shock-capturing schemes for this problem. The high resolution of the present method for this 1D shock–entropy interaction indicates that our scheme is efficient in distinguishing the high-frequency entropy waves from spurious oscillations.

Example 8. Results are now shown for the problem of Shu and Osher which also describes the interaction of an entropy sine wave with a Mach 3 right-moving shock. The computational domain is taken to be $[-1, 1]$ and the flow field is initialized with
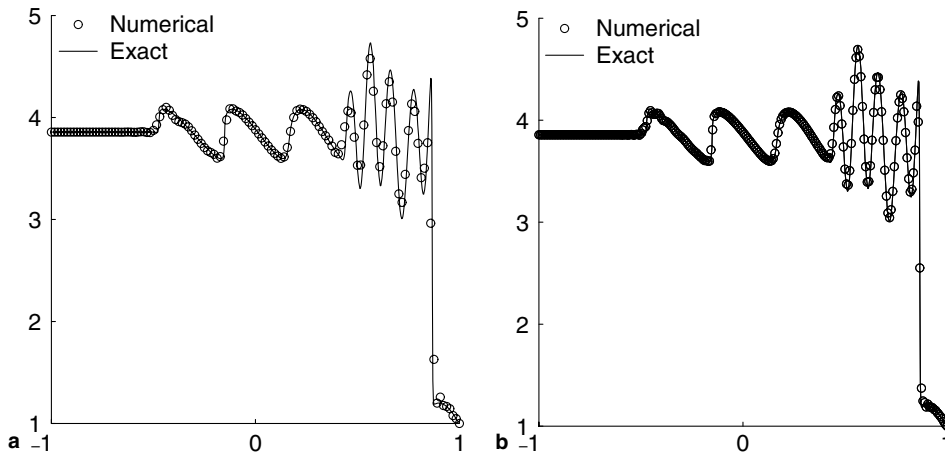
Fig. 13. Solution of the Shu-Osher problem ($t = 0.47$): (a) 127 cells; (b) 257 cells.

$$(\rho, u, p)_{t=0} = \begin{cases} (3.85714, 2.629369, 10.33333), & x \leqslant -0.8, \\ (1.0 + \epsilon \sin(\kappa \pi x), 0, 1.0), & x > -0.8, \end{cases} \tag{32}$$

where $\epsilon = 0.2$ and $\kappa = 5$. Obviously, this problem was designed to be a showcase for high order methods. However, it does not admit an exact solution. Figs. 13(a) and (b) depict the solutions of the density with 129 and 257 cells, respectively. The 'Exact' solution here is the solution computed by the fifth-order WENO [22] with 1200 cells. This problem involves non-monochromic waves and one cannot estimate the PPW value. The oscillatory nature of the problem makes it generally difficult for low order shock capturing schemes to compete with high order ones. As evident in the solution, the complicated flow field behind the shock is well resolved, and the shock front remains very sharp.

3.3. 2D Euler system

In two dimensions, the Euler equation for gas dynamics in a vector notation takes the conservation form

$$U_t + F(U)_x + G(U)_y = 0 \tag{33}$$

with

$$U = \begin{pmatrix} \rho \\ \rho u \\ \rho v \\ E \end{pmatrix}, \quad F(U) = \begin{pmatrix} \rho u \\ \rho u^2 + p \\ \rho uv \\ u(E + p) \end{pmatrix}, \quad G(U) = \begin{pmatrix} \rho v \\ \rho uv \\ \rho v^2 + p \\ v(E + p) \end{pmatrix}, \tag{34}$$

$$p = (\gamma - 1)\left[E - \frac{1}{2}\rho(u^2 + v^2)\right], \tag{35}$$

where (u, v) is the 2D fluid velocity, and $\gamma = 1.4$ is used in all computations. The conservative quantities, ρ, ρu, ρv and E are discretized on the mesh, and are filtered during the computation.

Example 9. As in the first 2D example, we use our Fourier pseudospectral scheme to study the interaction between a normal shock and a weak entropy wave which makes an angle $\theta \in (0, \pi/2)$ against the x-axis. If $\theta = 0$, we have essentially the 1D problem (i.e., Example 7). The initial conditions are defined as follows: the right state of the shock is given as $(\rho_r, u_r, v_r, p_r) = (1, 0, 0, 1)$ with a given shock Mach number $M_s = 3$. We add a small entropy wave to the flow on the right of the shock which is equivalent to changing only the density of the flow on the right of the shock. In our problem we change the density ρ_r in the right state of the shock by multiplying ρ_ϵ

$$\rho = \rho_{\mathrm{r}}\rho_{\epsilon},$$
$$\rho_{\epsilon} = \mathrm{e}^{-(\epsilon/p_{\mathrm{r}})\sin(\kappa(x\cos\theta + y\sin\theta))} \tag{36}$$

with ϵ and κ being the amplitude and wavenumber, respectively. In order to carry out a long time integration and to enforce the periodic boundary condition in the y-direction, the computational domain is taken to be $[0,9] \times [0, \frac{2\pi}{\kappa\sin\theta}]$. We initially position the normal shock at $x = 0.5$ and allow it to move up to $x = 8.5$. In our simulation, we adopt $\epsilon = 0.1$, $\kappa = 15$, and $\theta = 30°$. The performance is measured by the maximum amplitude of the amplified entropy waves in the y-direction for all fixed grid values $x \in [7.4, 8.4]$, and compared with the amplitude predicted by the linear analysis, i.e., 0.08744786.

We use 513 grid points in the x-direction and 32 grid points in the y-direction in our test. Fig. 14 displays the amplitudes of the amplified entropy waves. In order to avoid peak/valley losses of the entropy waves due to insufficient grid points near these positions, we interpolate our final results to a denser grid before we plot them. Obviously, the compressed entropy waves are well resolved in the post-shock regime even though small oscillations remain near the location of the shock. It is believed that such a trivial flaw is acceptable.

This example has further demonstrated the capability of our windowed Fourier pseudospectral scheme for capturing small scale waves in the presence of a shock.

Example 10. In this case, we investigate the advection of an isentropic vortex in a free stream. As the exact solution of this problem is available, it is a very good benchmark for examining the accuracy and stability of shock capturing schemes. In fact, this problem favors high order methods in terms of computational efficiency [11,55].

Consider a mean flow of $(\rho_{\infty}, u_{\infty}, v_{\infty}, p_{\infty}, T_{\infty}) = (1, 1, 1, 1, 1)$ with a periodic boundary condition in both directions. At t_0, the flow is perturbed by an isentropic vortex (u', v', T') centered at (x_0, y_0), having the form of

$$u' = -\frac{\lambda}{2\pi}(y - y_0)\mathrm{e}^{\eta(1 - r^2)}, \tag{37}$$

$$v' = \frac{\lambda}{2\pi}(x - x_0)\mathrm{e}^{\eta(1 - r^2)}, \tag{38}$$

$$T' = -\frac{(\gamma - 1)\lambda^2}{16\eta\gamma\pi^2}\mathrm{e}^{2\eta(1 - r^2)}. \tag{39}$$

Here, $r = \sqrt{(x - x_0)^2 + (y - y_0)^2}$ is the distance to the vortex center; λ is the strength of the vortex and η is a parameter determining the gradient of the solution. In our test, we choose $\lambda = 5$ and $\eta = 1$ unless we specify. Note that for an isentropic flow, relations $p = \rho^{\gamma}$ and $T = p/\rho$ are valid. Therefore, the perturbed ρ is required to be
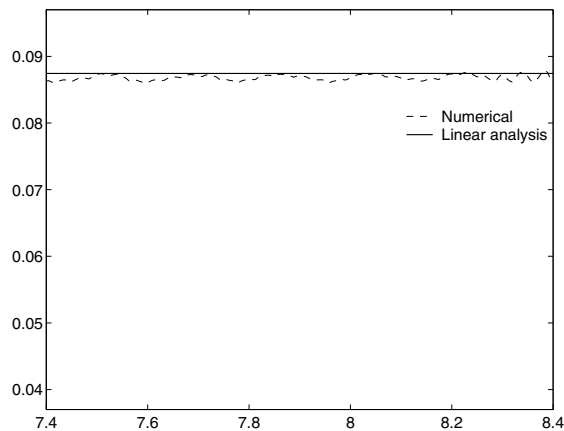

Fig. 14. The interaction of 2D shock and entropy waves ($N = 513$). The amplitude of entropy waves.

$$\rho = (T_\infty + T')^{1/(\gamma-1)} = \left[1 - \frac{(\gamma-1)\lambda^2}{16\eta\gamma\pi^2} e^{2\eta(1-r^2)} \right]^{1/(\gamma-1)}. \tag{40}$$

The computational domain is taken to be $[0, 10] \times [0, 10]$ with the center of the vortex being initially located at $(x_0, y_0) = (5, 5)$, i.e., the geometrical center of the computational domain.

Since there is no presence of shock in this problem, spectral method on its own can already provide excellent results if the time integration period is sufficiently short. As such, the DSC lowpass filter is not needed in the initial time period. However, as time progresses, errors would accumulate rapidly and the computation could become unstable if the lowpass filter is not activated to efficiently control the dramatical nonlinear growth of errors. In our numerical experiment which is not shown here, the integration blows up at around $t = 13$ if no filter is used.

Two experiments are conducted in this study. One is to examine the accuracy of our Fourier pseudospectral code and the other is to investigate the stability of our shock capturing scheme for a long time integration. For the first experiment, we compute the solution of ρ at the time $t = 2$ using three sets of meshes ($N = 32, 64, 128$). To make the spatial error dominant, we optimize the CFL number to be 0.01.

Two error measures, L_1 and L_2, have been used to evaluate the quality of the present method. To be consistent with the literature [11], two errors used in this problem are defined as

$$L_1 = \frac{1}{(N+1)^2} \sum_{i=0}^{N} \sum_{j=0}^{N} |f_{i,j} - \bar{f}_{i,j}|, \tag{41}$$

$$L_2 = \frac{1}{(N+1)} \sqrt{\sum_{i=0}^{N} \sum_{j=0}^{N} |f_{i,j} - \bar{f}_{i,j}|^2}, \tag{42}$$

where f is the numerical result and $\bar{f}$ the exact solution. Note that they are not the standard definitions. The errors for the density with respect to the exact solution are listed in Table 1 in which we also list the result of some other schemes for a comparison. As the table highlights, both the Fourier pseudospectral method and the local spectral DSC method [46,51] have the same order of accuracy. Up to 11th numerical order is observed for these two spectral approaches. It is also seen that both spectral methods are much more accurate than the fourth-order accurate, conservative central scheme (C4), which has numerically achieved its designed order. The reader is referred to a more comprehensive comparison in [11].

Our next numerical experiment concerns the performance of our pseudospectral code for the long time integration. Here, we compute the solution of ρ at the time $t = 100, 200, 400, 600, 800$ and 1000, with the grid $N = 64$. Note that we choose the gradient of the solution $\eta = 0.5$ in this case. We list L_1 and L_2 errors for the density in Table 2. It can be seen that our pseudospectral code is highly accurate even after such a long time evolution. The results indicate that our pseudospectral scheme together with the DSC wavelet lowpass filter is reliable for the numerical approximation of conservation laws.

Table 1
Advective 2D isentropic vortex

Mesh	Norm	FFT		C4		DSC	
		Error	Order	Error	Order	Error	Order
$N = 32$	L_1	5.58E − 5	–	1.96E − 3	–	1.27E − 4	–
	L_2	1.27E − 4	–	5.67E − 3	–	4.07E − 4	–
$N = 64$	L_1	2.33E − 8	11.23	1.32E − 4	3.89	8.18E − 8	10.60
	L_2	7.94E − 8	10.64	4.39E − 4	3.69	4.07E − 7	9.96
$N = 128$	L_1	4.01E − 11	9.18	8.90E − 6	3.89	3.99E − 11	11.00
	L_2	5.09E − 10	7.28	2.96E − 5	3.89	5.09E − 10	9.64

L_1 and L_2 errors for the density at $t = 2$. The CFL number is 0.01 for all schemes. C4 denotes the fourth-order accurate, conservative centered scheme.

Table 2
Advective 2D isentropic vortex

Mesh	Error	$t = 100$	$t = 200$	$t = 400$	$t = 600$	$t = 800$	$t = 1000$
$N = 64$	L_1	4.63E − 7	5.05E − 7	1.00E − 6	1.44E − 6	2.07E − 6	2.77E − 6
	L_2	1.99E − 6	1.23E − 6	2.90E − 6	4.42E − 6	6.02E − 6	7.59E − 6

L_1 and L_2 errors for the density at different times with $N = 64$ (CFL = 0.5, $\eta = 0.5$).

Example 11. This model problem describes the interaction between a stationary shock and a vortex. It has many potential applications and has been treated by many researchers using various techniques. Early numerical studies of this problem using spectral methods focused primarily on shock-fitting techniques. However, for cases in which a vortex causes a shock to deform at the point of bifurcation, it is generally difficult for a shock-fitting method to apply. This problem was successfully simulated in [6,8] by using the Chebyshev spectral method. In this work, we employ this model to assess the capability of the proposed Fourier pseudospectral shock-capturing method. The problem is defined as follows. The initialization is imposed on domain $[0,2] \times [0,1]$ with a stationary normal shock at $x = 0.5$, and a Mach 1.1 flow at the inlet. The right state of the shock is given as $(\rho_r, u_r, v_r, p_r) = (1, 1.1\sqrt{\gamma}, 0, 1)$. A vortex that is centered at $(x_c, y_c) = (0.25, 0.5)$ is generated by a perturbation to the velocity (u, v), temperature T and entropy S in the form

$$u' = \epsilon \tau e^{\alpha(1-\tau^2)} \sin \theta, \tag{43}$$

$$v' = -\epsilon \tau e^{\alpha(1-\tau^2)} \cos \theta, \tag{44}$$

$$T' = -\frac{(\gamma - 1)\epsilon^2 e^{2\alpha(1-\tau^2)}}{4\alpha\gamma}, \tag{45}$$

$$S' = 0, \tag{46}$$

where, $\tau = \frac{r}{r_c}$, $r = \sqrt{(x - x_c)^2 + (y - y_c)^2}$ and $\theta = \tan^{-1}[(y - y_c)/(x - x_c)]$. Here ϵ denotes the strength of the vortex, α is the decay rate of the vortex. Note that we can obtain perturbations in ρ and p according to the relations of $T = p/\rho$ and $S = \ln \frac{p}{\rho^\gamma}$. In our numerical experiment, we choose $\epsilon = 0.3$, $r_c = 0.05$ and $\alpha = 0.204$.

Reflective boundary conditions are imposed on both the upper and lower boundaries. We solve the Euler equation on a Cartesian grid of size 257×129, which is uniform in the y-direction and refined in the x-direction around the shock by using the Roberts transformation [2]. Once again, we emphasize that the DSC-RSK lowpass filter is used in the physical domain directly for this problem due to the presence of reflective boundaries. Figs. 15(a)–(e) show a time evolution of the shock–vortex interaction in terms of pressure contours. We can see that even at $t = 0.8$ the solution (Fig. 15(e)) is almost free of oscillations, and fine scale features are well captured. Particularly, the shock bifurcation reflected on the top boundary is shown clearly.

It is well known that the quality of results for the shock–vortex interaction can be evaluated by a quantitative comparison of circumferential pressure along the precursor of acoustic wave. In [41], the results of Hermite compact scheme (Hermite-6), ENO, modified ENO and WENO were presented, and were compared well with those of the Ribner theory [39]. In the present work, we choose the same parameters as those given in [41] to examine our spectral scheme and to compare with the Ribner theory [39]. A squared domain $[0,2] \times [0,2]$ is considered. The stationary shock is located at $x = 1.0$. The prescribed pressure jump through the shock is $\Delta P/P_\infty = 0.4$, where P_∞ is the static pressure at infinity, corresponding to a reference Mach number 1.29. The vortex is generated by a perturbation to the velocity (u, v), which have the same form as those in Eqs. (43) and (44), but with a counterclockwise rotation. The initial position of the vortex center is at $x_c = 0.5$, $y_c = 1.0$. The computation is performed with $\epsilon = 0.3$, $r_c = 0.075$ and $\alpha = 0.5$. The boundary conditions are the same as those in the previous case. A uniform Cartesian grid of the size of 257×257 is used in the computational domain.

Pressure contours at $t = 0.70$ are given in Fig. 16 in which the generated acoustic wave is seen clearly. The obtained circumferential pressure profile along the acoustic wave is compared with the analytical prediction of Ribner [39] in Fig. 17. It is seen that our result agrees well with the analytical one, though it exhibits a very small lagging error. For a more detailed comparison, the reader is referred to [41], where the results of many schemes were compared.
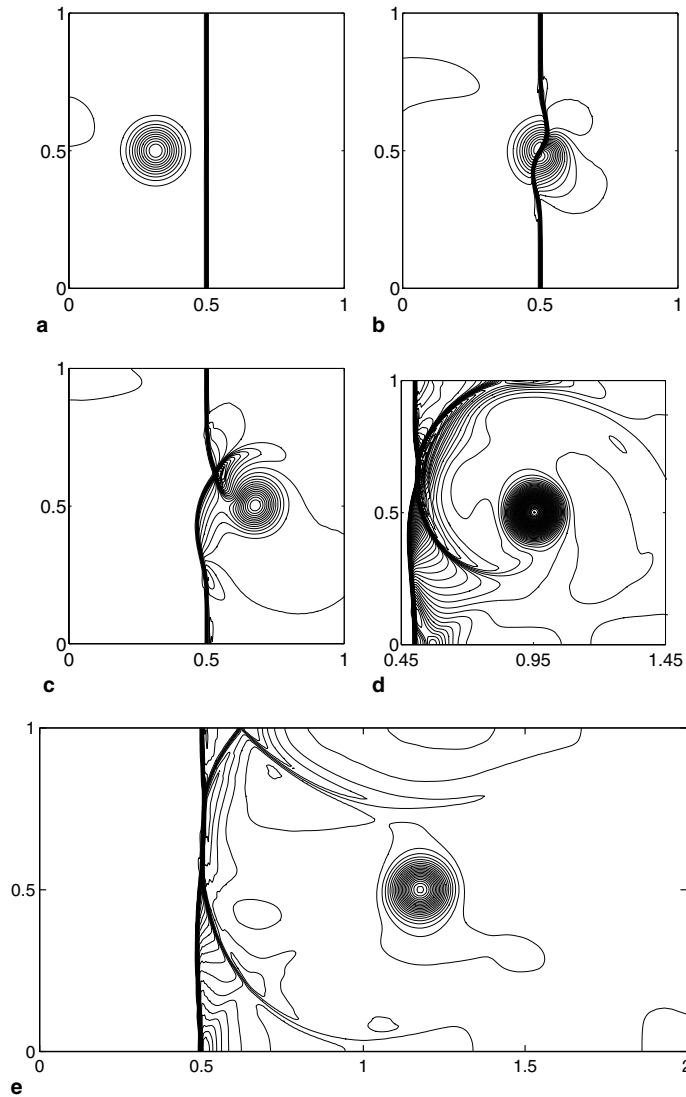
Fig. 15. The interaction of 2D shock and vortex (Mach = 1.1, $\epsilon = 0.3$, CFL=0.5). Pressure profiles. (a) $t = 0.05$, 30 contours; (b) $t = 0.20$, 30 contours; (c) $t = 0.35$, 30 contours; (d) $t = 0.60$, 90 contours from 1.01 to 1.37; (e) $t = 0.80$, 30 contours from 1.01 to 1.29.

In order to explore the potential of our algorithm for a strong shock, we increase the flow Mach number up to 3.0 and the strength of the vortex ϵ up to 0.6. The result at $t = 0.2$ is shown in Fig. 18. Deformation and bifurcation of the shock are observed clearly. This result indicates that the applicability of our spectral shock-capturing scheme is not limited to low Mach number and low vortex strength. Flows of high Mach number and high vortex strength can also be successfully simulated.

Example 12. Finally, we consider the problem of a supersonic flow past a cylinder [36]. This example is used to mainly examine the ability of our windowed spectral scheme in handling a non-rectangular domain.

The physical domain is on the x–y plane, and the computational domain is chosen to be $[0, 1] \times [0, 1]$ on the ξ–η plane. The mapping between the computational domain and the physical domain is

$$
\begin{aligned}
x &= -(R_x - (R_x - 1)\xi)\cos(\theta(2\eta - 1)), \\
y &= (R_y - (R_y - 1)\xi)\sin(\theta(2\eta - 1)),
\end{aligned}
\tag{47}
$$

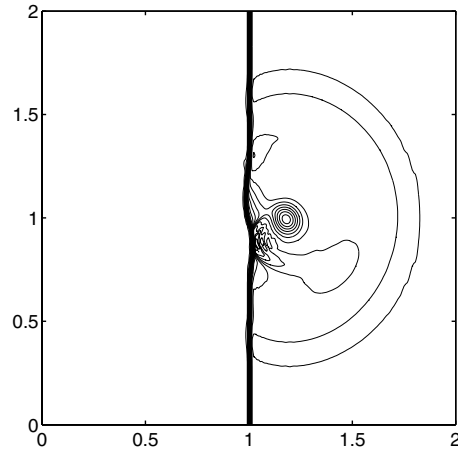where we take $R_x = 3$, $R_y = 6$ and $\theta = \frac{5\pi}{12}$.

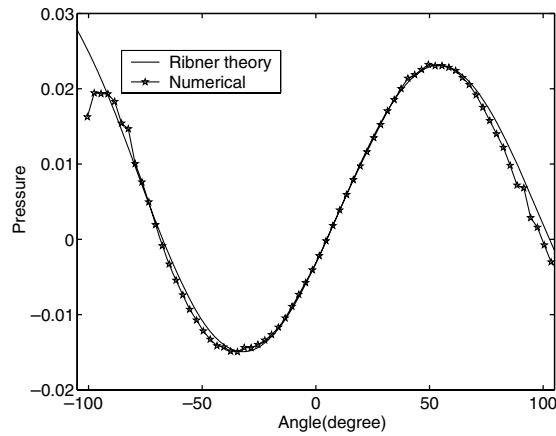Fig. 16. The interaction of 2D shock and vortex (Mach = 1.29). Pressure with 25 contours at $t = 0.70$.

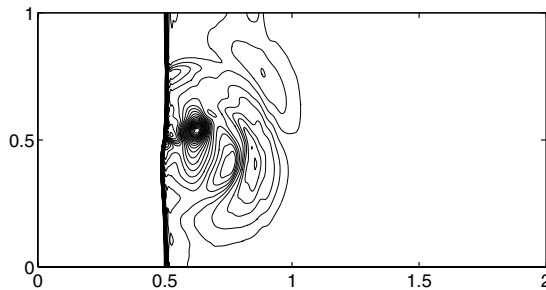Fig. 17. The circumferential pressure profile compared with the Ribner theory.

Fig. 18. The interaction of 2D shock and vortex ($t = 0.2$, Mach = 3.0, $\epsilon = 0.6$, CFL = 0.5). Pressure profiles.

An inlet flow of Mach number 2 is adopted with the state of $\rho = 1.0$, $u = 1.0$ and $v = 0$ [36]. We impose a reflective boundary condition on the surface of the cylinder, i.e., $\xi = 1$, and the outflow boundary condition at $\eta = 0$ and $\eta = 1$. A normal shock is generated in the front of the cylinder. It becomes steady after integration over a sufficiently long time.
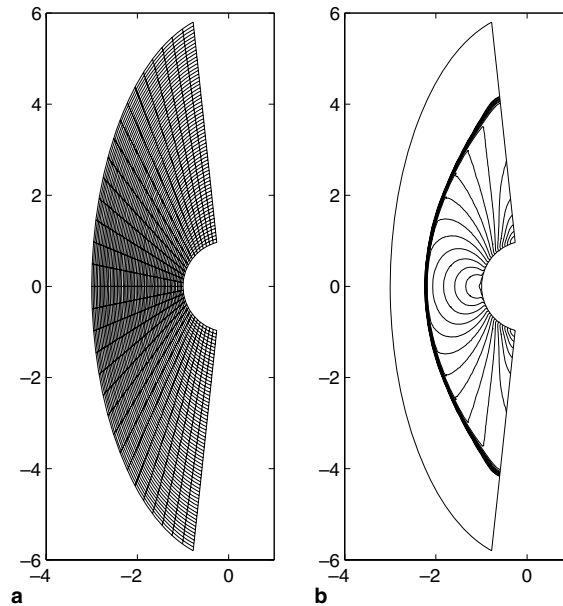
Fig. 19. Flow pass a cylinder: (a) physical grid; (b) pressure with 20 contours.

The reflective boundary condition is implemented as the follows. The velocity vector is decomposed into the ξ and η directions in the computational domain, i.e., $(u(\xi,\eta),v(\xi,\eta)) \rightarrow (V_\xi(\xi,\eta),V_\eta(\xi,\eta))$. Then, at each grid point, $(V_\xi(\xi,\eta),V_\eta(\xi,\eta))$ are assigned to the corresponding grid point in the extended domain, i.e., $(V_\xi(\xi_{N_\xi-1+i},\eta_j),V_\eta(\xi_{N_\xi-1+i},\eta_j)) = (-V_\xi(\xi_{N_\xi-1-i},\eta_j),V_\eta(\xi_{N_\xi-1-i},\eta_j))$, where $\xi_{N_\xi-1}=1$ is the location of the solid wall, $i=0,1,\ldots,N_\xi-1$ and $j=0,1,\ldots,N_\eta-1$. Finally, on the extended domain, vector components, $u(\xi,\eta)$ and $v(\xi,\eta)$ are computed, i.e., $(V_\xi(\xi,\eta),V_\eta(\xi,\eta)) \rightarrow (u(\xi,\eta),v(\xi,\eta))$, as they are the quantities needed in the Fourier transform.

In our simulation, a uniform mesh of 129×65 in the computation domain is used. Fig. 19(a) depicts a diagram of the mesh (drawing every other grid line) in the physical domain. Like the case on a rectangular domain, we double the computational domain in both ξ and η directions when we approximate the first order derivative of the flux using the Fourier pseudospectral method. The numerical result given in terms of pressure contours is shown in Fig. 19(b).

4. Discussion

From our numerical experiments it is found that the DSC lowpass filter is very effective not only in removing Gibbs oscillations produced by the spectral approximation, but also in restoring the high resolution feature of the Fourier pseudospectral method (FPM). Moreover, it is highlighted that this local spectral wavelet filter can dramatically improve the stability of the pseudospectral method in the long time integration. The main features of the proposed shock-capturing scheme are as follows:

- The basic scheme, the FPM, has the highest possible resolution of 2 points per wavelength (PPW), which is crucial to a class of physical problems involving high frequency waves. In particular, for problems that require not only capturing shock waves, but also resolving fine flow structures, a high resolution scheme is a must.
- Due to the use of FFT, the complexity of the proposed frequency domain shock-capturing scheme is of $O(N \ln N)$, because no additional operations are required to suppress Gibbs oscillations. This feature endows the proposed method with high efficiency, which is desirable for large scale problems in scientific and engineering applications.

- Numerical dissipation of the DSC filter is adjustable for a given problem, which enables the proposed method the flexibility to handle problems that are of different physical origins, and are sensitive to numerical dissipation. We consider this property as an essential feature because it has been shown in the literature [12] that many existing state of the art high order methods encounter difficulties in practical applications of different physical origins.
- The Fourier domain algorithm can be regarded as a windowed Fourier pseudospectral method (WFPM) for shock-capturing. The alternative use of the DSC filter in the physical domain makes the proposed method feasible to problems that require special boundary conditions, such as the reflective boundary condition.
- Comparing to other spectral methods that are designed for shock capturing, the WFPM uses uniform grids and avoids a strict stability constraint. This feature is similar to that of our previous local spectral CFOR scheme obtained from the Hermite polynomial expansion [55], which also admits a uniform grid.
- The proposed scheme by-passes the finding of the characteristics, which is required in many other shock-capturing schemes.
- Albeit only one- and two-dimensional problems are considered in this work, the use of the proposed method in higher dimensions is straightforward, via tensor product.
- The proposed scheme operates at 5 PPW for shock-capturing problems with periodic boundary conditions and 10 PPW for problems with non-periodic boundary conditions due to the double of the computational domain. Such a resolution is much higher than that of other commonly used high-order shock-capturing schemes. To our knowledge, the only other shock-capturing method that is able to operate at 5 PPW is the CFOR scheme proposed in our previous work [18,49,54,55]. We note that compact schemes could operate at similar resolutions for computing viscous flows with curvilinear grids.

As discussed earlier, there is no such a parameter r that is optimal to all problems. However, it is important to note that there are some patterns in the selection of parameter r, reflecting the nature of the physics under study. As listed in Appendix I, there are obviously two classes of r values. The first class of problems use r values ranging from 0.6 to 1.2. Whereas r values in the second class distribute from 2.0 to 3.2. The first class of problems includes Examples 1–6, and 12. A common feature in these problems is that there are only isolated discontinuities in their flow profiles. Their solutions consist of piecewise constants, piecewise linear polynomials, or low order polynomials. Their Fourier power spectral energies distributed mainly near the origin. For these problems, a small r value is required to focus the efficient frequency response of the local spectral wavelet lowpass filter to the vicinity of the origin. Such a lowpass filter causes the FPM to produce large amount of numerical dissipation. In fact, for this class of problems, high order methods, which are often more complicated, may require a longer running time and loss their advantages. Nonetheless, it remains to find out whether the proposed WFPM, with its complexity of $O(N \ln N)$, would be out performed by low order schemes in these problems.

The second class of problems, including Examples 7–11, all involve natural high frequency oscillations originated from the physics of each problem. In many cases, the physical oscillations or vortices interact with the shock front, and generate complicated flow patterns. It is for this class of problems, high order shock-capturing methods, including spectral approaches, find their great advantages over the low order ones. For these problems, their Fourier power spectral energies normally distribute over a wider range of frequencies. Therefore, a large r value is required to ensure that the natural physical oscillations and fine flow structures are well preserved under repeated filtering during the computation. Typically, low order methods are very expensive for these problems and require more than 50 PPW to resolve complex flow structures under the influence of the shock.

Based on the preceding analysis, we believe that it is advantageous for the proposed Fourier pseudospectral shock-capturing method to have an adjustable parameter so that a vast range of hyperbolic conservation law problems from different physical origins can be efficiently solved under a unified framework.

5. Conclusion

In this work, we introduce the use of local spectral wavelet filters, discrete singular convolution (DSC) lowpass filters [45–47], to the Fourier pseudospectral method (FPM) for the simulation of hyperbolic conservation

law systems. The fast Fourier transform (FFT) is used as the basic scheme, while DSC lowpass filters are adaptively used to suppress unphysical oscillations. The DSC filters are implemented in either the Fourier domain or the physical domain, depending on the boundary conditions of the physical problem under consideration. The Fourier domain implementation is easy and cost efficient, whereas the physical domain implementation allows more flexibility to handle some special boundary conditions. A sensor technique developed in the conjugate filter oscillation reduction (CFOR) scheme [18,49,54,55] is adopted in the present work to appropriately activate the DSC filter. The fourth-order Runge–Kutta scheme is utilized for the time integration. Extensive numerical experiments are considered to validate the proposed approach and to demonstrate its usefulness. Excellent numerical results are obtained for all the problems examined, and indicate that the proposed Fourier pseudospectral method has considerable potential for solving large scale problems in hyperbolic conservation law systems due to its high resolution and low complexity.

Acknowledgments

Appendix I

The values of r for DSC-RSK lowpass filters used in numerical experiments

No. of example	Case	r
1	$N = 128$	0.6
	$N = 256$	0.8
2	$N = 128$	0.6
	$N = 256$	0.8
3	$N = 129$	0.7
	$N = 257$	0.8
4	$N = 129$	0.6
	$N = 257$	0.6
5	$N = 65$	0.8
	$N = 129$	0.8
6	Lax	0.95
	Sod	1.1
7	$\kappa = 18$	2.2
	$\kappa = 36$	2.2
	$\kappa = 54$	2.1
8	$N = 129$	2.0
	$N = 257$	2.1
9		2.1
10	$\eta = 1.0$	3.2
	$\eta = 0.5$	2.8
11		2.8
12		1.2

References

[1] S. Abarbanel, D. Gottlieb, E. Tadmor, Spectral methods for discontinuous problems, in: K. Morton, M. Baines (Eds.), Numerical Methods for Fluid Dynamics, Oxford University Press, New York, 1986, pp. 129–153.

[2] D.A. Anderson, J.C. Tannehill, R.H. Pletcher, Computational Fluid Mechanics and Heat Transfer, McGraw-Hill, New York, 1984.

[3] F. Bianco, G. Puppo, G. Russo, High-order central differencing for hyperbolic conservation laws, SIAM J. Sci. Comput. 21 (1999) 294–322.

[4] J.P. Boyd, Chebyshev and Fourier Spectral Methods, second ed., Dover, New York, 2000.

[5] W. Cai, D. Gottlieb, C.-W. Shu, Essentially nonoscillatory spectral Fourier methods for shock wave calculations, Math. Comput. 52 (186) (1989) 389–410.

[6] W. Cai, C.-W. Shu, Uniform high-order spectral methods for one- and two-dimensional Euler equations, J. Comput. Phys. 104 (1993) 427–443.

[7] C. Canuto, M.Y. Hussaini, A. Quarteroni, T.A. Zang, Spectral Methods in Fluid Dynamics, Springer, Berlin, 1988.

[8] W.S. Don, Numerical study of pseudospectral methods in shock wave applications, J. Comput. Phys 110 (1994) 103–111.

[9] W.S. Don, D. Gottlieb, Spectral simulation of supersonic reactive flows, SIAM J. Numer Anal. 35 (1998) 2370–2384.

[10] B. Fornberg, A Practical Guide to Pseudospectral Methods, Cambridge University Press, Cambridge, 1996.

[11] E. Garnier, P. Sagaut, M. Deville, A class of explicit ENO filters with application to unsteady flows, J. Comput. Phys. 170 (2001) 184–204.

[12] E. Garnier, M. Mossi, P. Sagaut, P. Comet, M. Deville, On the use of shock-capturing scheme for large-eddy simulation, J. Comput. Phys. 153 (2001) 273–311.

[13] D. Gottlieb, L. Lustman, S.A. Orszag, Spectral calculations of one-dimensional inviscid compressible flow, SIAM J. Sci. Stat. Comput. 2 (1981) 296–310.

[14] D. Gottlieb, E. Tadmor, Recovering pointwise values of discontinuous data within spectral accuracy, in: Earll M. Murman, Saul S. Abarbanel (Eds.), Progress and Supercomputing in Computational Fluid Dynamics, Birkhäuser, Basel, 1985, pp. 357–375.

[15] D. Gottlieb, C.-W. Shu, A. Solomonoff, H. Vandeven, On the Gibbs phenomenon I, J. Comput. Appl. Math. 43 (1992) 81–98.

[16] D. Gottlieb, J.S. Hesthaven, Spectral methods for hyperbolic problems, J. Comput. Appl. Math. 128 (2001) 83–131.

[17] T. Grahs, T. Sonar, Entropy-controlled artificial anisotropic diffusion for the numerical solution of conservation laws based on algorithms from image processing, J. Vis. Commun. Image R 13 (2002) 176–194.

[18] Y. Gu, G.W. Wei, Conjugated filter approach for shock capturing, Commun. Numer. Meth. Eng. 19 (2003) 99–110.

[19] A. Harten, B. Engquist, S. Osher, S. Chakravarthy, Uniform high-order accurate essentially non-oscillatory schemes, III, J. Comput. Phys. 131 (1997) 3–47.

[20] D.J. Hill, D.I. Pullin, Hybrid tuned center-difference-WENO method for large eddy simulations in the presence of strong shocks, J. Comput. Phys. 194 (2004) 435–450.

[21] M.Y. Hussaini, D.A. Kopriva, M.D. Salas, T.A. Zang, Spectral methods for the Euler equation: Part I – Fourier methods and shock-capturing, AIAA J. 23 (1) (1985) 64–70.

[22] G.-S. Jiang, C.-W. Shu, Efficient implementation of weighted ENO schemes, J. Comput. Phys. 126 (1996) 202.

[23] S. Jin, C.D. Levermore, Numerical schemes for hyperbolic conservation laws with stiff relaxation terms, J. Comput. Phys. 126 (1996) 449–467.

[24] S.T. Johansen, J.Y. Wu, W. Shyy, Filter-based unsteady RANS computations, Int. J. Heat Fluid Flow 25 (2004) 10–21.

[25] R. Krasny, A study of singularity formation in a vortex sheet by the point vortex approximation, J. Fluid Mech. 167 (1986) 65–93.

[26] A. Kurganov, D. Levy, A third-order semidiscrete central scheme for conservation laws and convention diffusion equations, SIAM J. Sci. Comput. 22 (2000) 1461–1488.

[27] F. Lafon, S. Osher, High order filtering methods for approximating hyperbolic systems of conservation laws, J. Comput. Phys. 172 (1992) 574–591.

[28] S. Lee, S.K. Lele, P. Moin, Interaction of isotropic turbulence with shock waves: effect of shock strength, J. Fluid Mech. 340 (1997) 225–247.

[29] R.J. LeVeque, M. Pelanti, A class of approximate Riemann solvers and their relation to relaxation schemes, J. Comput. Phys. 172 (2001) 574–591.

[30] X.-D. Liu, E. Tadmor, Third order non-oscillatory central scheme for hyperbolic conservation laws, Numer. Math. 79 (1998) 397–425.

[31] S.G. Li, D. McLaughlin, H.S. Liao, A computationally practical method for stochastic groundwater modeling, Adv. Water Resour. 26 (2003) 1137–1148.

[32] S.G. Li, D.B. McLaughlin, Using nonstationary spectral method for analyzing groundwater flow in heterogeneous trending media, Water Resour. Res. 31 (1995) 541–551.

[33] A. Majda, J. McDonough, S. Osher, The Fourier method for nonsmooth initial data, Math. Comput. 32 (1978) 1041–1081.

[34] L.S. Mulholland, D.M. Sloan, The effect of filtering on the pseudospectral solution of evolutionary partial differential equation, J. Comput. Phys. 96 (1991) 369–390.

[35] H. Nessyahu, E. Tadmor, Non-oscillation central differencing for hyperbolic conservation laws, J. Comput. Phys. 87 (1990) 408–463.

[36] P. Nithiarasu, O.C. Zienkiewicz, B.V.K.S. Sai, K. Morgan, R. Codina, M. Vazquez, Shock capturing viscosities for the general fluid mechanics algorithm, Int. J. Numer. Meth. Fluids 28 (1998) 1325–1353.

[37] L.W. Qian, On the regularized Whittaker–Kotel'nikov–Shannon sampling formula, Proc. Am. Math. Soc. 131 (2003) 1169–1176.

[38] J.-X. Qiu, C.-W. Shu, On the construction, comparison, and local characteristic decomposition for high order central WENO schemes, J. Comput. Phys. 183 (2002) 187–209.

[39] H.S. Ribner, Cylindrical sound wave generated by shock–vortex interaction, AIAA J. 23 (11) (1985) 1708–1715.

[40] E. Tadmor, Convergence of spectral methods for nonlinear conservation laws, SIAM J. Numer. Anal. 26 (1989) 30–44.

[41] C. Tenaud, E. Garnier, P. Sagaut, Evaluation of some high-order shock capturing schemes for direct numerical simulation of unsteady two-dimensional free flows, Int. J. Numer. Meth. Fluids 33 (2000) 249–278.

[42] E.F. Toro, R.C. Millington, V.A. Titarev, ADER: arbitrary-order non-oscillatory advection scheme, in: Proceedings of the 8th International Conference on Non-linear Hyperbolic Problems, Magdeburg, Germany, March, 2000.

[43] L.N. Trefethen, Spectral Methods in Matlab, Oxford University Press, Oxford, England, 2000.

[44] H. Vandeven, Family of spectral filters for discontinuous problems, J. Sci. Comput. 6 (1991) 159–192.

[45] D.C. Wan, B.S.V. Patnaik, G.W. Wei, Discrete singular convolution-finite subdomain method for the solution of incompressible viscous flows, J. Comput. Phys. 180 (2002) 229–255.

[46] G.W. Wei, Discrete singular convolution for the solution of the Fokker–Planck equations, J. Chem. Phys. 110 (1999) 8930–8942.

[47] G.W. Wei, Y.B. Zhao, Y. Xiang, Discrete singular convolution and its application to the analysis of plates with internal supports. I. Theory and algorithm, Int. J. Numer. Meth. Eng. 55 (2002) 913–946.

[48] G.W. Wei, Oscillation reduction by anisotropic diffusions, Comput. Phys. Commun. 144 (2002) 317–342.

[49] G.W. Wei, Y. Gu, Conjugated filter approach for solving Burgers' equation, J. Comput. Appl. Math. 149 (2002) 439–456.

[50] K. Xu, A gas-kinetic BGK scheme for the Navier–Stokes equations and its connection with artificial dissipation and Godunov method, J. Comput. Phys. 171 (2001) 289–335.

[51] S.Y. Yang, Y.C. Zhou, G.W. Wei, Comparison of the discrete singular convolution algorithm and the Fourier pseudospectral method for solving partial differential equations, Comput. Phys. Commun. 143 (2002) 113–135.

[52] H.C. Yee, N.D. Sandham, M.J. Djomehri, Low-dissipative high-order shock-capturing methods using characteristic-based filters, J. Comput. Phys. 150 (1999) 199–238.

[53] S.N. Yu, S. Zhao, G.W. Wei, Local spectral time splitting method for first and second order partial differential equations, J. Comput. Phys. 206 (2005) 727–780.

[54] Y.C. Zhou, Y. Gu, G.W. Wei, Shock-capturing with natural high frequency oscillations, Int. J. Numer. Methods Fluid 41 (2003) 1319–1338.

[55] Y.C. Zhou, G.W. Wei, High resolution conjugate filters for the simulation of flows, J. Comput. Phys. 189 (2003) 159–179.